

Submitted to *Ceramics International*, June 2011.

On the oxidation of ZrB₂ powders during high-energy ball-milling in air

Angel L. Ortiz*, Victor Zamora, Fernando Rodríguez-Rojas

Departamento de Ingeniería Mecánica, Energética y de los Materiales,

Universidad de Extremadura, 06006 Badajoz, Spain

Abstract

Oxide impurities in ZrB₂ powders promote coarsening, resulting in lower sinterability. Given its importance for sintering, we studied the oxidation of ZrB₂ powders during high-energy ball-milling (the form of milling able to refine ZrB₂ powders to the nanoscale) with the aid of a wide battery of characterization techniques, namely fusion in inert gas, X-ray diffractometry, helium pycnometry, transmission electron microscopy, and Fourier-transform infrared, Raman, and X-ray photoemission spectroscopy. It was found that high-energy ball-milling in air introduces twice as much oxygen into the ZrB₂ powders as the more conventional attrition milling. Also, this oxygen does not form solid-solutions with ZrB₂, but amorphous oxides (i.e., ZrO₂ and B₂O₃) that locate preferentially on the surface of the ultra-fine agglomerates resulting from cold-welding of the primary nano-particles that form during the ball-milling. The implications of these findings for the field of ultra-high-temperature ceramics are discussed.

Keywords: ZrB₂; ultra-high-temperature ceramics; high-energy ball-milling.

* Corresponding author:

Angel L. Ortiz

Phone: +34 924289600 Ext: 86726

Fax: +34 924289601

E-mail: alortiz@materiales.unex.es

1. Introduction

It has been demonstrated that the refinement of the starting powders and the elimination of surface oxide impurities are two key processing steps to enhance the solid-state sinterability of the poorly sinterable ZrB_2 powders that are being used to process ultra-high-temperature ceramics (UHTCs) [1-7]. The reduction in the particle size shortens the diffusion distance of the chemical species, thus speeding up the densification kinetics significantly for the interparticle-diffusion controlled sintering [8], something that is especially relevant in ZrB_2 due to the serious kinetic restrictions imposed by its strong covalent bonding and its low self-diffusion coefficients [9]. It is not surprising therefore that the typical micrometre-sized ZrB_2 particles need to be refined to the submicrometre range before the sintering heat-treatment. With respect to surface oxide impurities in non-oxide ceramics, they are known to favour the evaporation–condensation mass transport mechanism [10], and this promotes coarsening thus reducing the driving force for densification and limiting the final density [10]. Hence, it is necessary to remove the surface oxides of ZrO_2 and B_2O_3 in ZrB_2 at temperatures below which coarsening is significant (1650–1850 °C) to thus retain the original particle size up to the temperatures where densification can proceed.

In most studies on ZrB_2 UHTCs, the starting powders are refined by wet attrition milling using some alcohol or inert organic solvent as liquid media [3,4]. Under these wet operating conditions, attrition milling is actually conventional ball-milling because the liquid media reduces the milling intensity, so that its function is only comminution (i.e., particle size reduction). The typical ZrB_2 particles achieved by attrition milling have submicrometre sizes (between 0.6 and 0.2 μm), much smaller than the micrometre-sized particles ($\sim 2 \mu m$) of the commonest commercially-available ZrB_2 powders. The current practice used to remove the surface oxides of ZrO_2 consists of adding to the ZrB_2 powders sintering additives with the potential to act as reducing agents, the most widely used of which are C, B_4C , and WC [1,2,5,11]. The removal of B_2O_3 from the surface of ZrB_2 is by evaporation, simply maintaining an actively pumped vacuum at temperatures below 1650 °C [2,6]. Apart from the intrinsic surface oxide layer in the ZrB_2 particles, further oxidation of the ZrB_2 powder occurs during the attrition milling. Typically, between 1 and 2 wt.% oxygen is introduced during attrition milling under flowing argon gas atmosphere, and a little bit more (i.e., ~ 2 wt.%) if the milling is conducted in air [1-3,6,7,11-14].

1
2
3
4 Recently, it has been shown that high-energy ball-milling in dry conditions using shaker
5 mills can refine the ZrB_2 powders to the nanoscale [15-17], something that conventional ball-
6 milling cannot do. This is because the mechanism of crystal size refinement in ZrB_2 is brittle
7 fracture, where the fracture strength scales inversely with the square root of the crystal size [18],
8 and the compressive stresses generated during the high-energy ball-milling are high enough (i.e.,
9 GPa) to fracture fine particles [19,20]. This refinement to the nanoscale offers unprecedented
10 opportunities to enhance sintering kinetics immensely, as has been demonstrated lately [21]. An
11 aspect that has received no attention to date despite its importance is the oxidation of the ZrB_2
12 powders during high-energy ball-milling in air. Predicting this oxidation a priori is difficult
13 because high-energy ball-milling times are fairly short (~3 h) relative to attrition milling times
14 (~24 h), which contributes to minimizing the oxidation, whereas the milling intensity is much
15 higher and the nano-particles are more air-sensitive, which factors have the opposite effect.
16

17
18 With these premises in mind, the present study was undertaken with the objective of
19 investigating the oxidation of ZrB_2 powders induced by their high-energy ball-milling in air,
20 because milling in air would simplify the routine of powder preparation. The study includes
21 determination of the oxygen uptake, and the structural and chemical statuses of the captured
22 oxygen.
23
24

25 26 27 28 29 30 31 32 33 34 35 36 37 **2. Experimental Procedure** 38

39 The starting powder was a commercially-available micrometre ZrB_2 powder with 99%
40 purity and single-crystal particles of average size 2 μm . The as-purchased ZrB_2 powder was
41 subjected to high-energy ball-milling using a shaker mill (Spex D8000, Spex CertiPrep,
42 Metuchen, NJ, US) operated at about 1060 back-and-forth cycles per minute. The milling was
43 carried out in a cylindrical hardened-steel container with WC balls (6.7 mm in diameter) at a
44 ball-to-powder weight ratio of 4, for 180 min, in air. Subsequently, the ball-milled powder was
45 analyzed using a wide variety of characterization techniques: transmission electron microscopy
46 (TEM) for the direct examination of the size and morphology of the powder particles and nano-
47 crystals, inert gas fusion (IGF) for the determination of the oxygen uptake, X-ray diffractometry
48 (XRD) for the identification of the amorphous or crystalline nature of the phases present, helium
49 pycnometry for the measurement of the density, and Fourier-transform infrared (FTIR), Raman,
50
51
52
53
54
55
56
57
58
59
60
61
62
63
64
65

1
2
3
4 and X-ray photoemission (XPS) spectroscopy for the determination of the bonding environment
5 or status.
6

7
8 The TEM observations were made at 200 kV in bright-field mode, using two
9 conventional microscopes (Tecnai G² 20 Twin, FEI, Eindhoven, The Netherlands; and JEM-
10 2100, JEOL, Croissy-sur-Seine, France). The oxygen content measurements were done with an
11 IGF determinator (TC-136, Leco Instrument, St. Joseph, MI, US) using graphite crucibles,
12 helium gas, and Ni as flux. The XRD data were collected in step-scanning mode (step width
13 0.02° 2 θ , and count time 3 s/step) using a high-resolution laboratory diffractometer (D8
14 Advance, Bruker AXS, Karlsruhe, Germany) equipped with a primary monochromator that
15 provides pure CuK α ₁ radiation ($\lambda = 1.54183 \text{ \AA}$) and a linear ultra-fast detector. Two
16 measurement ranges were employed: 20–80°, and 20–55°. The phases present were identified
17 with the aid of the PDF2 database, and were quantified using the Rietveld method (Topas 4.1,
18 Bruker AXS, Karlsruhe, Germany). The density measurements were made by helium
19 pycnometry (Stereopycnometer, Quantachrome Instruments, Hartley Wintney, UK). The FTIR
20 spectra were recorded in the 4000–400 cm⁻¹ range on a conventional spectrophotometer (Nicolet
21 iS10, Thermo Scientific, East Grinstead, UK), using the KBr pellet method and an accumulation
22 condition of 60 scans at 1 cm⁻¹ resolution. The Raman spectra were measured in the 1000–125
23 cm⁻¹ range using a micro-Raman spectrometer (Nicolet Almega XR, Thermo Scientific)
24 equipped with a 633 nm He–Ne laser operated at 5.25 mW power, and were the result of 10
25 accumulations lasting 1 s. The XPS spectra of the Zr 3d and B 1s core lines were recorded in
26 ultra-high vacuum (10⁻⁶ Pa) in the 176–194 eV range at 0.4 eV energy resolution using a high-
27 resolution spectrometer (K-Alpha, Thermo Scientific) equipped with a monochromatic Al-K α X-
28 ray source (1486.6 eV). The C 1s peak was used to correct the binding energies in the XPS
29 spectra. The protocol of sample preparation for each of these techniques followed standard
30 procedures for ceramic powders.
31
32
33
34
35
36
37
38
39
40
41
42
43
44
45
46
47
48
49
50

51 **3. Results and Discussion**

52
53
54 Figure 1 compares representative TEM images of the as-purchased ZrB₂ powder and of
55 the ZrB₂ powder ball-milled for 180 min in air. Clearly, the high-energy ball-milling has reduced
56 the particle size by one order of magnitude from the micrometre scale (~2–3 μm) to the
57 nanometre scale (~120–200 nm). Furthermore, higher-magnification TEM images such as that
58
59
60
61
62
63
64
65

1
2
3
4 shown in Fig. 2 indicate that the powder particles after high-energy ball-milling are actually
5 porous agglomerates consisting of many individual tiny single-crystals with an average size of
6 ~10 nm.
7
8

9
10 The oxygen contents determined by IGF were 1.537 and 4.514 wt.% for the as-purchased
11 and ball-milled ZrB₂ powders, respectively, so that one can conclude that there is an oxygen
12 uptake of ~3 wt.% during the high-energy ball-milling in air. This oxygen content is greater than
13 those typically reported for ZrB₂ powders prepared by attrition milling which are normally in the
14 2–3 wt.% range depending on the exact milling conditions [1-3,6,7,11-14]. To explore the
15 structural and chemical statuses of the oxygen captured during the high-energy ball-milling in
16 air, an exhaustive characterization of the ball-milled powder was needed, as we shall describe
17 next.
18
19

20
21
22
23
24 Figure 3 compares the XRD patterns of the ZrB₂ powder before and after the high-energy
25 ball-milling for 180 min in air. Apart from the reduction in the peak intensity, the marked peak
26 broadening, and the increase in the background after the high-energy ball-milling that together
27 reflect the crystallite size refinement to the nanoscale (~10 nm), and the presence of additional
28 peaks that reveal the introduction of 2.5 wt% of WC according to the corresponding Rietveld
29 analysis, there are another two important features in the figure. The first is that the ZrB₂ peaks
30 remain in place. Since the absence of peak shifting excludes the formation of solid-solutions with
31 oxygen atoms as solutes in the ZrB₂ host, it can be concluded that the oxygen captured during the
32 high-energy ball-milling in air has formed oxides. The second is the absence of ZrO₂ and/or
33 B₂O₃ peaks in the XRD patterns of the ball-milled ZrB₂ powder. Taking this observation together
34 with the previous one, one can conclude that these oxides are amorphous. One could nevertheless
35 argue that it would be very difficult to detect B₂O₃ by XRD in the presence of ZrB₂ because the
36 scattering factor of Zr will dominate the entire diffractogram. Nevertheless, ZrO₂ should be
37 detected which would prove the oxidation via the reaction $\text{ZrB}_2 + 5/2 \text{O}_2(\text{g}) \rightarrow \text{ZrO}_2 + \text{B}_2\text{O}_3$ if
38 this oxidation reaction had resulted in crystalline oxides. It could also be argued that crystalline
39 ZrO₂ and B₂O₃ are formed during the high-energy ball-milling in air, but at amounts below the
40 XRD detection limit. However, given the oxygen content determined by IGF and assuming
41 equimolar formation of ZrO₂ and B₂O₃ as predicted by the above reaction, their concentrations is
42 estimated to be 6.95 and 3.93 wt.%, respectively, which are clearly high enough to be detected
43 by XRD. To prove that this is indeed the case, two powder mixtures in which 1 wt.% crystalline
44
45
46
47
48
49
50
51
52
53
54
55
56
57
58
59
60
61
62
63
64
65

1
2
3
4 ZrO₂ was added to ZrB₂ were prepared and analyzed by XRD. In one of these two mixtures the
5
6 crystals had submicrometre sizes and in the other nanometre sizes, done so as to rule out any
7
8 crystallite-size effect in the detection of crystalline ZrO₂ in ZrB₂-based powders. It can be seen in
9
10 Fig. 4 that, despite the low ZrO₂ concentration of only 1 wt.%, the XRD patterns of these
11
12 mixtures exhibit clear peaks of this oxide. Hence, these observations confirm that the oxide
13
14 concentration deduced from IGF is above the detection limit of the diffractometer, and therefore
15
16 that the oxides formed during high-energy ball-milling in air are amorphous because otherwise
17
18 they would have been detected.

19
20 Despite its non-crystalline nature, the amorphous-phase content in the ball-milled ZrB₂
21
22 powder can be estimated from its XRD pattern using the Rietveld method in conjunction with the
23
24 spiking technique (known crystallinity internal-standard method). In the present study, 30 wt.%
25
26 Al₂O₃ was used as the spike phase because it provides a sufficient number of peaks in the XRD
27
28 pattern with no overlap with the ZrB₂ peaks, and because its oxide nature rules out the presence
29
30 of a passivating amorphous layer. With this XRD analysis, as shown in Fig. 5, the amorphous-
31
32 phase content in the ball-milled ZrB₂ powder was calculated to be 12 wt.%, which is clearly
33
34 consistent with the oxide concentration (i.e., ZrO₂+B₂O₃) determined by IGF (~11 wt.%).

35
36 The measurements of the powder density performed by helium pycnometry also lend
37
38 strong credence to the formation of amorphous oxides, as they show that the density decreases
39
40 from 6.12 g·cm⁻³ in the as-purchased condition to 5.82 g·cm⁻³ after 180 min of high-energy ball-
41
42 milling in air. Using the rule-of-mixture with the values of theoretical density and volume
43
44 concentrations determined experimentally of ZrB₂ (6.1 g·cm⁻³, 86.94 wt.%), WC (17.67 g·cm⁻³,
45
46 2.23 wt.%), ZrO₂ (5.86 g·cm⁻³, 6.91 wt.%) and B₂O₃ (2.46 g·cm⁻³, 3.93 wt.%), the density of the
47
48 ball-milled powder was calculated to be 5.826 g·cm⁻³, in perfect agreement with the experimental
49
50 measurement.

51
52 To further investigate the formation of amorphous ZrO₂ and B₂O₃ during the high-energy
53
54 ball-milling of ZrB₂ in air, FTIR and Raman spectroscopy studies were conducted with the aim
55
56 of detecting the vibration bands of the Zr–O and B–O bonds. Shown in Figs. 6 and 7 are,
57
58 respectively, the FTIR and Raman spectra of the as-purchased and ball-milled ZrB₂ powders,
59
60 together with the spectra of ZrO₂ and B₂O₃ powders that were also collected experimentally and
61
62 included for comparison. As can be seen in Fig. 6, not only are the FTIR spectra from the two
63
64 ZrB₂ powders similar, but neither do they exhibit the vibration bands typical of ZrO₂ and B₂O₃.
65

1
2
3
4 As shown in Fig. 7, this scenario is also valid for the Raman spectra, despite ZrB_2 not being
5 Raman active [22] which in principle should have facilitated the detection of the Raman peaks of
6 ZrO_2 and B_2O_3 . Thus, it can be concluded that the FTIR and Raman spectroscopic studies are
7 unable to conclusively discriminate the presence of the concentrations of ZrO_2 and B_2O_3 formed
8 during the high-energy ball-milling of ZrB_2 in air.
9

10
11 To confirm the formation of amorphous oxides as deduced from the XRD, IGF and
12 helium pycnometry analyses, the as-purchased and ball-milled ZrB_2 powders were investigated
13 by XPS, which is a spectroscopic technique with a far better detection limit than FTIR or Raman
14 spectroscopy. In particular, we monitored the binding energy of the Zr 3d and B 1s core levels
15 before and after the high-energy ball-milling for 180 min in air (Fig. 8). One observes that the Zr
16 3d core level shows the typical $3d_{5/2}$ and $3d_{3/2}$ spin-orbit split, while the B 1s core level exhibits
17 the typical single peak. However, two Zr $3d_{5/2}$ - $3d_{3/2}$ doublets and two B 1s singlets are observed
18 in each powder, which is a clear sign of the existence of two different bonding statuses for the Zr
19 and B atoms. In both the as-purchased and the ball-milled powders, one set of Zr $3d_{5/2}$ - $3d_{3/2}$
20 doublets plus B 1s singlet is located at binding energies of ~179.2, 181.6, and 188.2 eV,
21 respectively, values which are due to ZrB_2 [23,24]. The other set of doublets plus singlet appears
22 at higher binding energies of ~183.5, 185.9, and 193.1 eV, respectively, which are due to ZrO_2
23 and B_2O_3 [23,24]. One also observes that the $\text{ZrO}_2/\text{ZrB}_2$ and $\text{B}_2\text{O}_3/\text{ZrB}_2$ peak intensity ratios are
24 greater in the powder subjected to high-energy ball-milling in air. Therefore, XPS has
25 unambiguously detected the presence of ZrO_2 and B_2O_3 in the as-purchased and ball-milled ZrB_2
26 powders, and also shows them to be much more abundant in the ball-milled powder. Also noted
27 in the XPS spectra of the two powders is that the ZrO_2 related peaks are more intense than the
28 ZrB_2 related peaks. This observation, together with the oxygen contents that showed that the
29 oxides are minor components and the fact that XPS is a surface technique, indicate that ZrO_2 and
30 B_2O_3 cover the surface of the ZrB_2 particles. This hypothesis was further tested experimentally in
31 the ball-milled powder by etching the surface with Ar^+ ions to remove material, followed by XPS
32 data collection and by TEM. One observes in Fig. 9 that the $\text{ZrB}_2/\text{ZrO}_2$ and $\text{ZrB}_2/\text{B}_2\text{O}_3$ peak
33 intensity ratios increase after the etching, a clear sign that the ZrB_2 powder particles are covered
34 by an oxide layer. As can be seen in Fig. 10, the direct high-resolution TEM observations also
35 support the presence of an amorphous nano-film at the fringe of the agglomerates. This oxide
36 distribution is attributed to two factors: (i) the lower chemical affinity between the oxides and
37
38
39
40
41
42
43
44
45
46
47
48
49
50
51
52
53
54
55
56
57
58
59
60
61
62
63
64
65

1
2
3
4 ZrB₂ than between ZrB₂ crystals themselves which would promote cold-welding during the high-
5 energy ball-milling via contacts of the type ZrB₂-ZrB₂; and (ii) the spontaneous surface
6 passivation of ball-milled powder particles when exposed to ambient conditions after the high-
7 energy ball-milling.
8
9

10
11 Despite the greater oxygen content of these powders compared with those prepared by
12 attrition milling, high-energy ball-milling in air is likely to offer unprecedented opportunities to
13 enhance the sinterability of ZrB₂, and probably of other UHTCs. This is because of its unique
14 potential to produce ultra-fine agglomerates of primary nano-particles with a large inter-particle
15 boundary surface area.^a This expectation has indeed recently been confirmed in a spark-plasma
16 sintering study of ZrB₂ powders with different intensities of high-energy ball-milling in air [21],
17 and it is consistent with earlier studies showing that the oxygen impurities do not hinder
18 densification of ZrB₂ by spark-plasma sintering or hot-pressing [7]. It is also believed that the
19 greater oxygen content in the powders subjected to high-energy ball-milling in air will not inhibit
20 their densification by pressureless sintering, unlike the case with powders subjected to attrition
21 milling [7], although this has yet to be confirmed experimentally. This expectation derives from
22 the anticipation that: (i) the green density of the compacts made from these agglomerates can be
23 relatively high if sufficient pressure is applied during the cold compaction because the ultra-fine
24 agglomerate size can improve the powder packing density; and (ii) the large inter-particle
25 boundary area can greatly enhance grain-boundary diffusion at lower temperatures in
26 comparison with powder particles of the same size as the agglomerates but with no internal grain
27 boundaries and less oxygen content. Of course, one would expect the sinterability of ZrB₂
28 powders to improve even further if the high-energy ball-milling were performed in an inert
29 atmosphere, although the comminution routine would be more tedious and costly.
30
31
32
33
34
35
36
37
38
39
40
41
42
43
44
45
46
47
48
49

4. Concluding remarks

50 We have described an investigation of the oxidation of ZrB₂ powders during their high-
51 energy ball-milling in air, using a wide battery of analytical techniques. The direct measurement
52 of the oxygen content by the IGF method revealed that the powders subjected to high-energy
53 ball-milling in air are twice as rich in oxygen as those subjected to the more conventional
54
55
56
57
58

59 ^a Taking an average agglomerate size of 200 nm and a primary particle size of 10 nm with the assumption of
60 spherical agglomerates, the inter-particle boundary area per unit volume within each agglomerate is $1.67 \times 10^7 \text{ m}^{-1}$.
61
62
63
64
65

1
2
3
4 attrition milling. The XRD analyses, including detailed Rietveld refinements, showed that the
5 captured oxygen does not form solid-solutions but amorphous oxides. The density measurement
6 by helium pycnometry confirmed the formation of such oxides, and was entirely consistent with
7 the phase composition determined by IGF and XRD. The XPS analyses indicated that these
8 amorphous oxides are ZrO_2 and B_2O_3 , something that could not be determined by the FTIR or
9 Raman spectroscopy, and that that they locate preferentially on the surface of the powder
10 particles, in perfect agreement with the direct TEM observations. Finally, we suggested that
11 high-energy ball-milling in air may have an important role to play in the fabrication of ZrB_2
12 UHTCs because the processing routine is simplified and the resulting nano-powders are expected
13 to exhibit improved sinterability despite their greater oxygen content.
14
15
16
17
18
19
20
21
22
23

24 **Acknowledgements** This work was supported by the Ministerio de Ciencia y Tecnología
25 (Government of Spain) under Grant N° MAT 2007-61609.
26
27
28
29
30
31
32
33
34
35
36
37
38
39
40
41
42
43
44
45
46
47
48
49
50
51
52
53
54
55
56
57
58
59
60
61
62
63
64
65

References

- 1) A.L. Chamberlain, W.G. Fahrenholtz, G.E. Hilmas, Pressureless sintering of zirconium diboride, *J. Am. Ceram. Soc.* 89 (2) (2006) 450–456.
- 2) S.C. Zhang, G.E. Hilmas, W.G. Fahrenholtz, Pressureless densification of zirconium diboride with boron carbide additions, *J. Am. Ceram. Soc.* 89 (5) (2006) 1544–1550.
- 3) W.G. Fahrenholtz, G.E. Hilmas, I.G. Talmy, J.A. Zaykoski, Refractory diborides of zirconium and hafnium, *J. Am. Ceram. Soc.* 90 (5) (2007) 1347–1364.
- 4) S.-Q. Guo, Densification of ZrB₂-based composites and their mechanical and physical properties: a review, *J. Eur. Ceram. Soc.* 29 (6) (2009) 995–1011.
- 5) S. Zhu, W.G. Fahrenholtz, G.E. Hilmas, S. Zhang, Pressureless sintering of zirconium diboride using boron carbide and carbon additions, *J. Am. Ceram. Soc.* 90 (11) (2007) 3660–3663.
- 6) W.G. Fahrenholtz, G.E. Hilmas, S.C. Zhang, S. Zhu, Pressureless sintering of zirconium diboride: particle size and additive effects, *J. Am. Ceram. Soc.* 91 (5) (2008) 1398–1404.
- 7) M. Thompson, W.G. Fahrenholtz, G. Hilmas, Effect of starting particle size and oxygen content on densification of ZrB₂, *J. Am. Ceram. Soc.* 94 (2) (2011) 429–435.
- 8) C. Herring, Effect of change of scale on sintering phenomena, *J. Appl. Phys.* 21 (4) (1950) 301–303.
- 9) R. Telle, L.S. Sigl, K. Takagi, Boride-Based Hard Materials; pp. 802–945 in *Handbook of Ceramic Hard Materials*, Vol. 2, Edited by R. Riedel. Wiley-VCH, Weinheim, 2000.
- 10) S.L. Dole, S. Prochazka, R.H. Doremus, Microstructural coarsening during sintering of boron carbide, *J. Am. Ceram. Soc.* 72 (6) (1989) 958–966.
- 11) S. Zhu, W.G. Fahrenholtz, G.E. Hilmas, S.C. Zhang, Pressureless sintering of carbon-coated zirconium diboride powders, *Mat. Sci. Eng. A* 459 (1-2) (2007) 167–171.
- 12) H. Zhang, Y. Yan, Z. Huang, X. Liu, D. Jiang, Pressureless sintering of ZrB₂-SiC ceramics: the effect of B₄C content, *Scripta Mater.* 60 (7) (2009) 559–562.
- 13) S.C. Zhang, G.E. Hilmas, W.G. Fahrenholtz, Mechanical properties of sintered ZrB₂-SiC ceramics, *J. Eur. Ceram. Soc.* 31 (5) (2011) 893–901.
- 14) X.-G. Wang, W.-M. Guo, G.-J. Zhang, Pressureless sintering mechanism and microstructure of ZrB₂-SiC ceramics doped with boron, *Scripta Mater.* 61 (2) (2009) 177–180.
- 15) C.A. Galán, A.L. Ortiz, F. Guiberteau, L.L. Shaw, Crystallite size refinement of ZrB₂ by

- 1
2
3
4 high-energy ball milling, *J. Am. Ceram. Soc.* 92 (12) (2009) 3114–3117.
5
6 16) C.A. Galán, A.L. Ortiz, F. Guiberteau, L.L. Shaw, High-energy ball milling of ZrB₂ in the
7 presence of graphite, *J. Am. Ceram. Soc.* 93 (10) (2010) 3072–3075.
8
9 17) V. Zamora, A.L. Ortiz, F. Guiberteau, M. Nygren, L.L. Shaw, On the crystallite size
10 refinement of ZrB₂ by high-energy ball-milling in the presence of SiC, *J. Eur. Ceram. Soc.*
11 (2011), in press.
12
13 18) B.R. Lawn, *Fracture of brittle solids*. Cambridge University Press. Cambridge, UK; 1993.
14
15 19) C. Suryanarayana, Mechanical alloying and milling, *Prog. Mater. Sci.* 46 (1-2) (2001) 1–184.
16
17 20) P.R. Soni, *Mechanical alloying. Fundamental and applications*. Cambridge International
18 Science Publishing. Cambridge, UK; 2001.
19
20 21) V. Zamora, A.L. Ortiz, F. Guiberteau, M. Nygren, Crystal-size dependence of the spark-
21 plasma-sintering kinetics of ZrB₂ ultra-high-temperature ceramics, *J. Eur. Ceram. Soc.*
22 (2011), submitted.
23
24 22) J. Watts, G. Hilmas, W.G. Fahrenholtz, D. Brown, B. Clausen, Measurement of thermal
25 residual stresses in ZrB₂–SiC composites, *J. Eur. Ceram. Soc.* 31 (9) (2011) 1811–1820.
26
27 23) L. Huerta, A. Durán, R. Falconi, M. Flores, R. Escamilla, Comparative study of the core level
28 photoemission of the ZrB₂ and ZrB₁₂, *Physica C* 470 (9-10) (2010) 456–460.
29
30 24) D. Alfano, L. Scatteia, F. Monteverde, E. Bêche, M. Balat-Pichelin, Microstructural
31 characterization of ZrB₂–SiC based UHTC tested in the MESOX plasma facility, *J. Eur.*
32 *Ceram. Soc.* 30 (11) (2010) 2345–2355.
33
34
35
36
37
38
39
40
41
42
43
44
45
46
47
48
49
50
51
52
53
54
55
56
57
58
59
60
61
62
63
64
65

1
2
3
4
5
6
Figure Captions

7
8
9
10
11
Figure 1. TEM bright-field images of the ZrB₂ powder particles (a) in the as-purchased condition, and (b) after high-energy ball-milling for 180 min in air.

12
13
14
15
16
17
18
Figure 2. TEM bright-field image of the interior of the ZrB₂ powder particles with 180 min of high-energy ball-milling in air, showing the agglomeration and cold-welding of individual primary nano-particles with 10 nm size.

19
20
21
22
23
24
25
Figure 3. XRD patterns of the ZrB₂ powders before and after high-energy ball-milling for 180 min in air. The WC peaks free of overlap with ZrB₂ peaks are marked. The logarithmic scale is to facilitate appreciation of the WC peaks.

26
27
28
29
30
31
32
33
34
Figure 4. XRD patterns of the ZrB₂+1 wt.% ZrO₂ powder mixtures with coarse crystals and with nano-crystals. The WC peaks free of overlap with ZrB₂ peaks are marked. The position of the ZrO₂ peaks is marked with short vertical lines. The logarithmic scale is to facilitate appreciation of the ZrO₂ and WC peaks.

35
36
37
38
39
40
41
Figure 5. Rietveld analysis of the XRD pattern of the ZrB₂ powder with 180 min of high-energy ball-milling in air plus 30 wt.% of Al₂O₃ powder. The points are the experimental data and the solid line is the Rietveld refinement.

42
43
44
45
46
47
48
49
50
Figure 6. FTIR spectra of the ZrB₂ powders before and after high-energy ball-milling for 180 min in air. The FTIR spectra of ZrO₂ and B₂O₃ have been included for comparison. The bands at ~2350, 1400 and 670 cm⁻¹ and the noise at 3900-3650 and 1830-1430 cm⁻¹ are due to background.

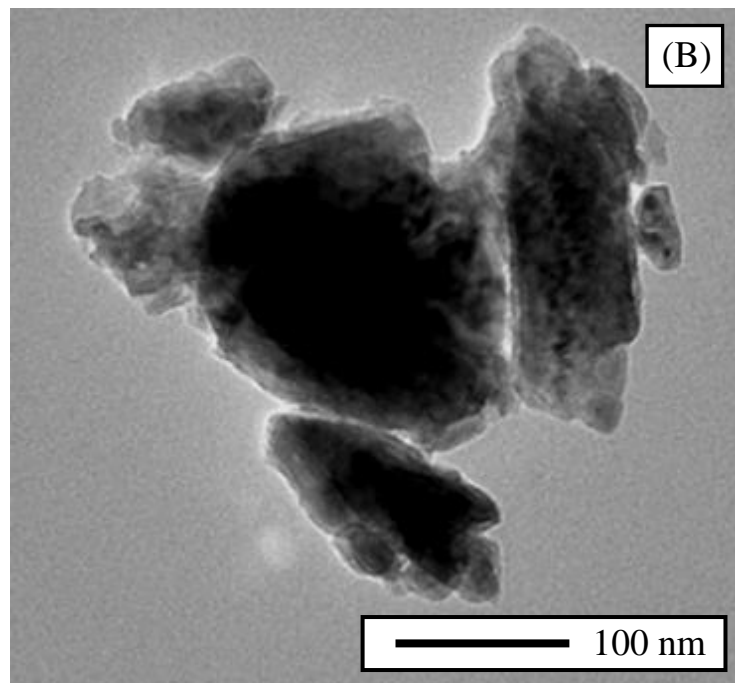
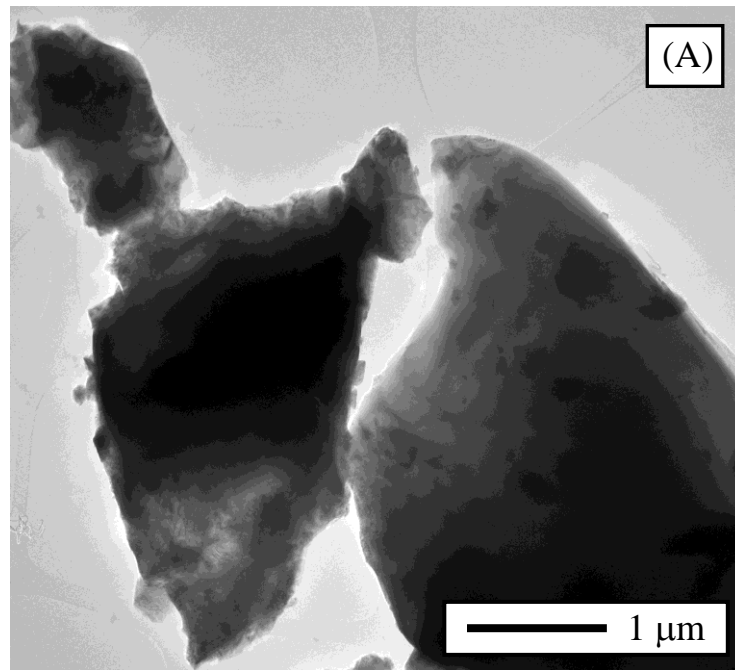
51
52
53
54
55
Figure 7. Raman spectra of the ZrB₂ powders before and after high-energy ball-milling for 180 min in air. The Raman spectra of ZrO₂ and B₂O₃ have been included for comparison.

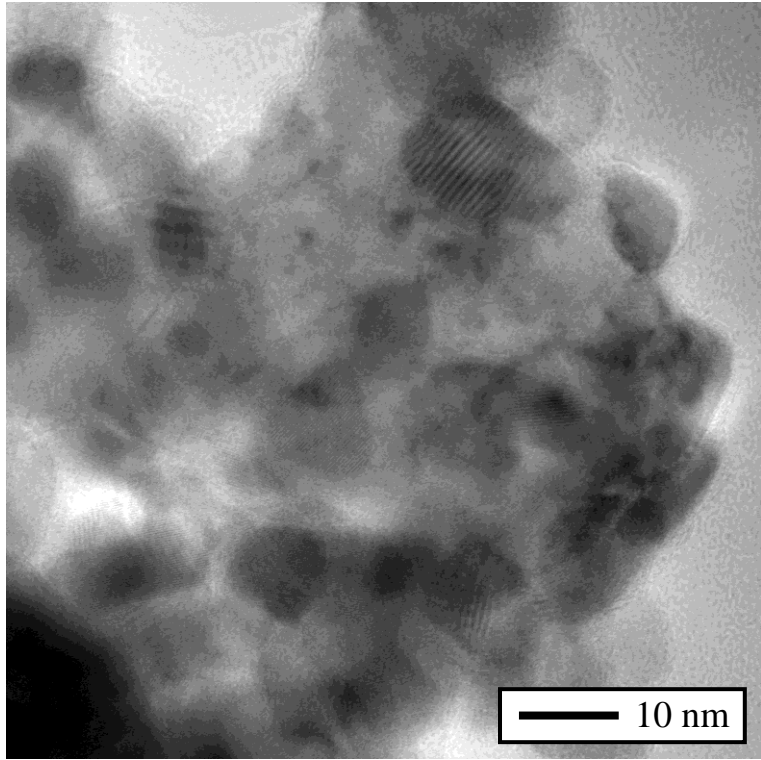
56
57
58
59
60
61
62
63
64
65
Figure 8. High-resolution XPS spectra of the Zr 3d and B 1s core-levels for the ZrB₂ powders before and after high-energy ball-milling for 180 min in air. Also included in the figure is the peak indexing. The spectra have been shifted along the Y-axis to facilitate comparison.

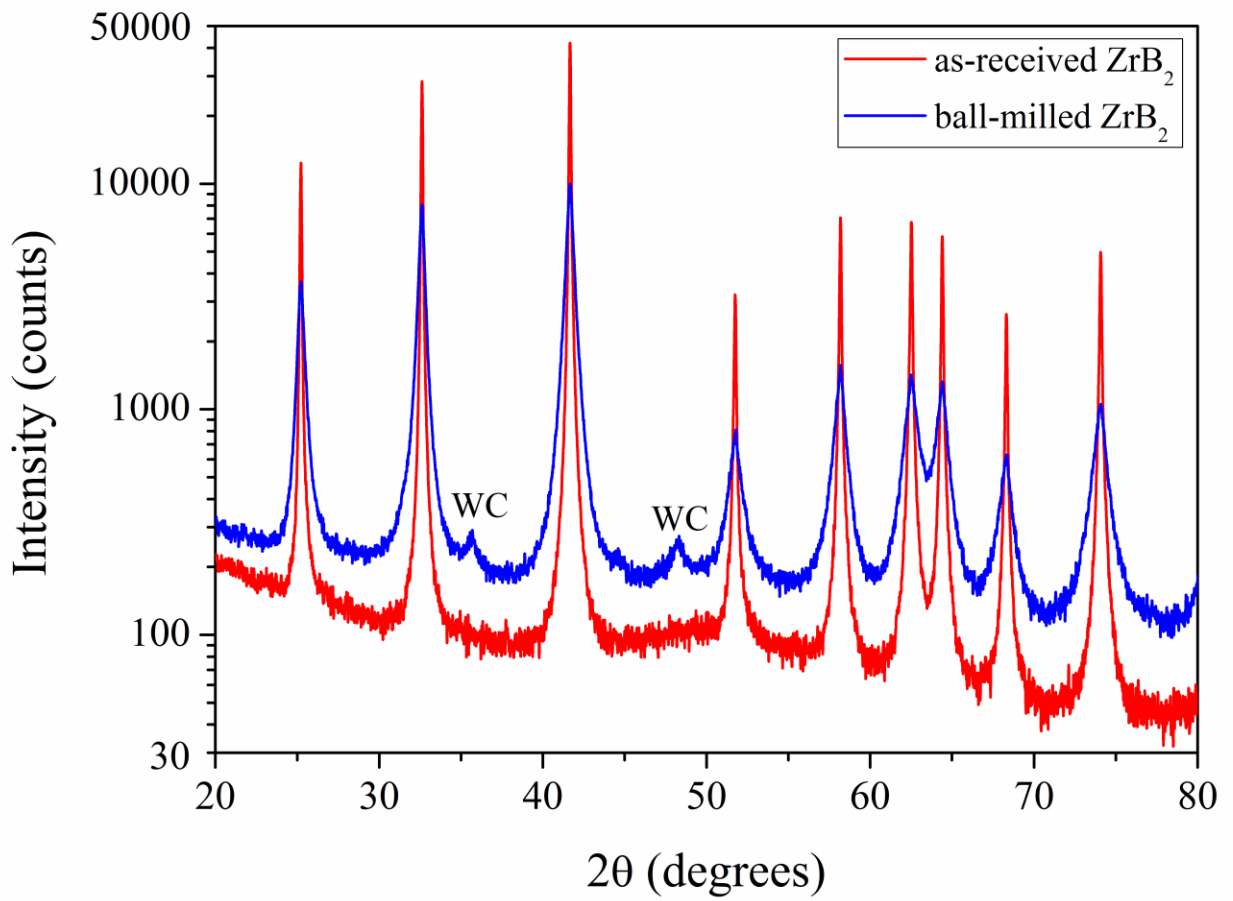
1
2
3
4
5
6
7
8
9
10
11
12
13
14
15
16
17
18
19
20
21
22
23
24
25
26
27
28
29
30
31
32
33
34
35
36
37
38
39
40
41
42
43
44
45
46
47
48
49
50
51
52
53
54
55
56
57
58
59
60
61
62
63
64
65

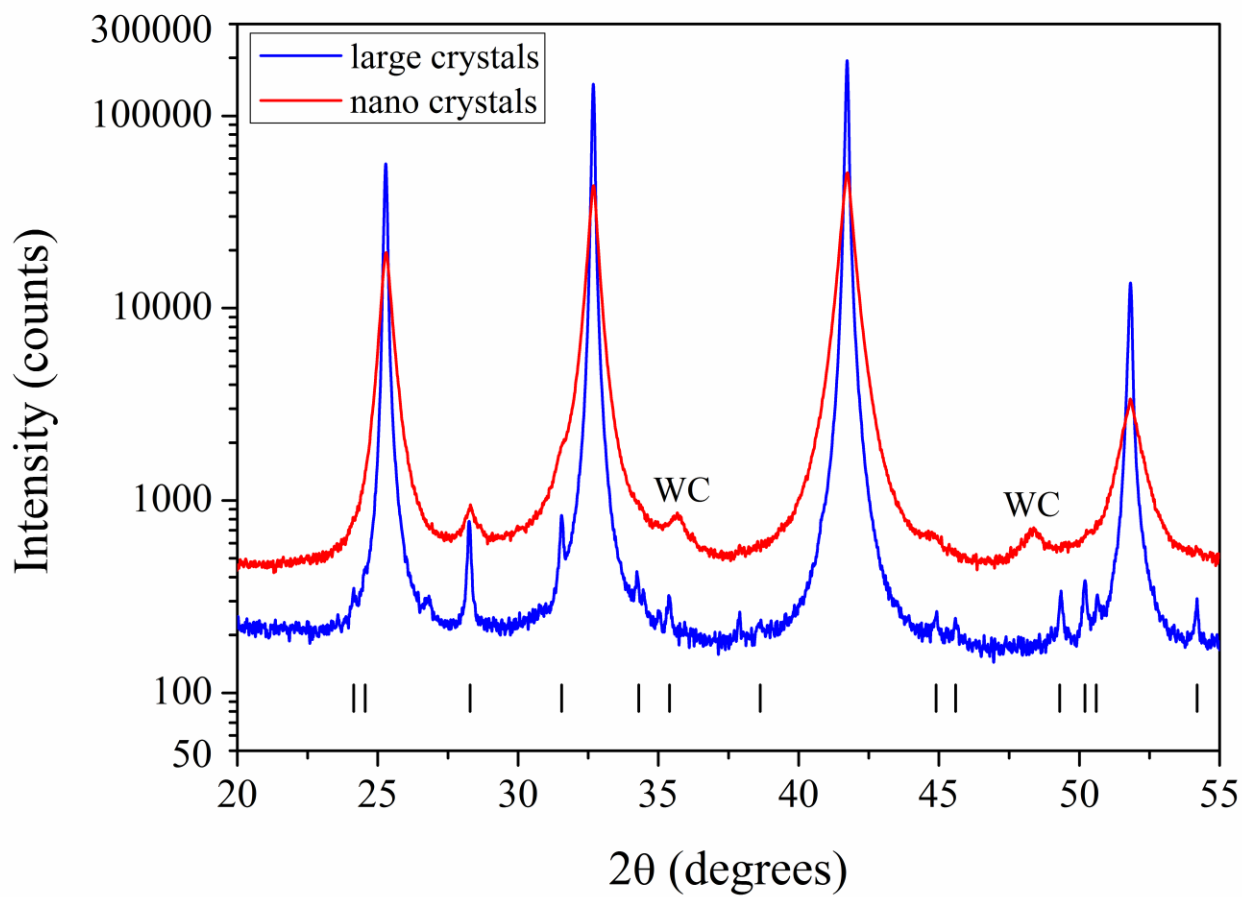
Figure 9. High-resolution XPS spectra of the Zr 3d and B 1s core-levels for the ZrB₂ powders with 180 min of high-energy ball-milling in air before and after etching with Ar⁺ ions. Also included in the figure is the peak indexing. The spectra have been shifted along the Y-axis to facilitate comparison.

Figure 10. High-resolution TEM bright-field image of the fringe of the ZrB₂ powder particles with 180 min of high-energy ball-milling in air, showing the presence of an amorphous region of nanometric thickness.

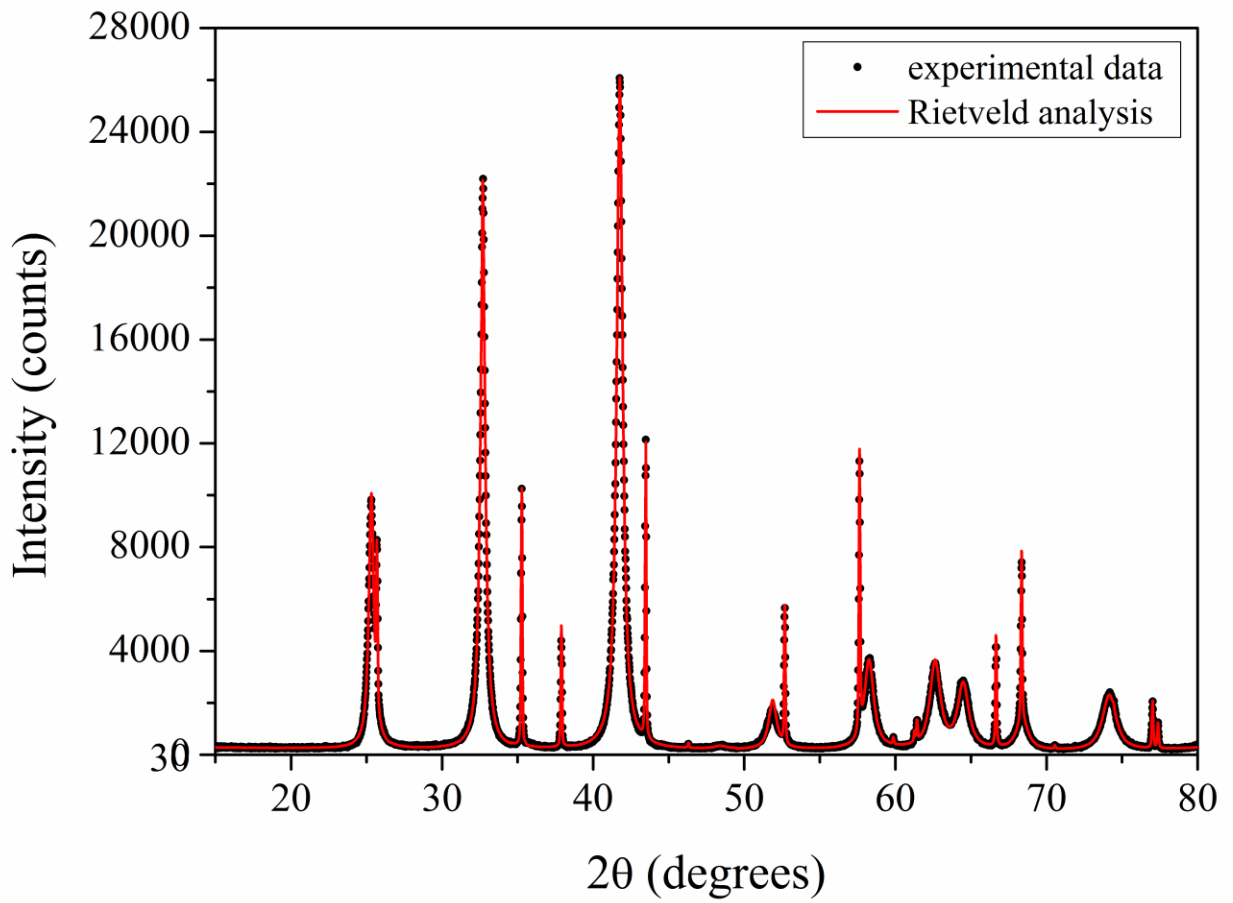


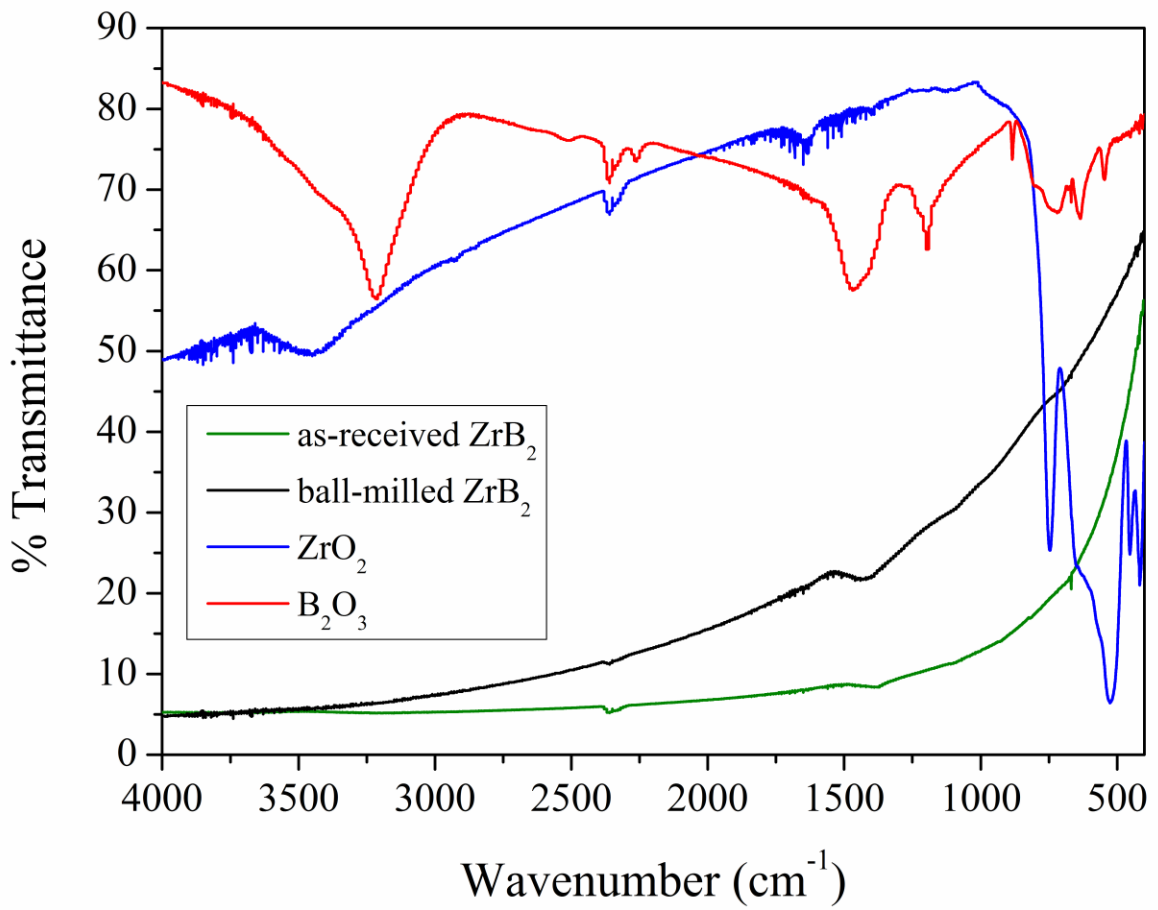






Ortiz *et al.*
Figure 4





Ortiz *et al.*
Figure 6

